Simple and efficient volume merging method for triply periodic minimal structures☆

Yibao Li [a], Qing Xia [a], Sungha Yoon [b], Chaeyoung Lee [b], Bingheng Lu [c,d], Junseok Kim [b,*]

[a] *School of Mathematics and Statistics, Xi'an Jiaotong University, Xi'an 710049, China*
[b] *Department of Mathematics, Korea University, Seoul 02841, Republic of Korea*
[c] *Collaborative Innovation Center of High-End Manufacturing Equipment, Xi'an Jiaotong University, Xi'an 710049, China*
[d] *National Institute of Additive Manufacturing, Xi'an 710049, China*

A R T I C L E   I N F O

A B S T R A C T

Triply periodic minimal surfaces (TPMSs), which are periodic in all three directions and are surfaces of zero mean curvature, have been proven experimentally to be highly suitable for tissue scaffolds. However, simply gluing different TPMS units with different porosities and pore sizes could induce discontinuous structures and destroy the physical properties. In this study, we propose a simple and efficient volume merging method for triply periodic minimal structures. The proposed method can be divided into two steps. The first step is a novel merging algorithm for unit triply periodic minimal structures in the implicit function framework. The composite scaffold can be designed by merging different unit structures to satisfy the properties of internal connectivity. The second step is to optimize the designed composite scaffolds to satisfy the properties of TPMSs. A modified Allen–Cahn-type equation with a correction term is proposed. The mean curvature on the surface is constant at all points in the equilibrium state. Typically, the obtained structure is smooth owing to the motion by mean curvature flow. Therefore, the quality of the structure is significantly improved. Based on the operator splitting method, the proposed algorithm consists of two analytical evaluations for the ordinary differential equations and one numerical solution for the implicit Poisson-type equation. The proposed numerical scheme can be applied in a straightforward manner to a GPU-accelerated discrete cosine transform (DCT) implementation, which can be executed multiple times faster than CPU-only alternatives. Computational experiments are presented to demonstrate the efficiency and robustness of the proposed method.

1. Introduction

An artificial bone should consist of bio-compatible and bio-active porous scaffolds to replace the natural skeleton. In general, biological porous scaffolds should satisfy the following characteristics [1]: (i) three-dimensional (3D) porous structures with interconnections and connected pores for the transport of nutrients and metabolic waste; (ii) biocompatible with artificial regulatory mechanism for degradation and resorption; (iii) suitable environmental protection for cell division, proliferation and differentiation; (iv) proper mechanical performance to match the tissues at the site of transplantation. Such characteristics make it difficult to manufacture biological porous scaffolds using traditional methods. Additive manufacturing (AM) is a fabrication method that allows precise control over the architecture and scales of constructed tissue scaffolds [2–4].

The fabrication of biological scaffolds using AM technology has attracted considerable attention [5–7]. Chua et al. [8] studied suitable polyhedral shapes that can be applied to tissue scaffolds, and subsequently classified the unit cells. They developed a tissue engineering scaffold library for AM [9]. Puppi et al. [10] generated an AM technique for fabricating 3D polymeric scaffolds. In their research, two different scaffold models were fabricated by tuning the inter-fiber distance and fibers staggering that demonstrated acceptable reproducibility. Hollister et al. [11] proposed an image-based design based on computed tomography or magnetic resonance image data for the reconstruction of a defect. It used a Boolean combination of defect and architecture images to create a 3D scaffold image. Xie and Steven [12] proposed an optimization method to generate porous structures with maximum bulk and shear moduli, which demonstrated faster convergence and unambiguous material definition. Implicit surface modeling, which uses a single mathematical equation to freely generate
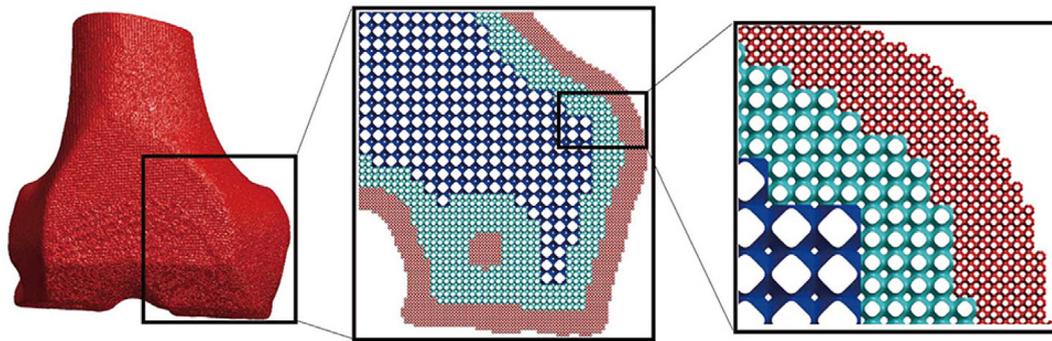
Fig. 1. Multi-scale fabrication with variable porosity in the patella.

pore shapes, such as triply periodic minimal surfaces (TPMSs), provides a new method for designing tissue scaffolds [2,13,14].

TPMSs have been proven experimentally to be highly suitable for tissue scaffolds [15,16]. The inherent porosity of the TPMS-type model can represent the natural morphology of polymers and macromolecules [3]. Using TPMS structures to create cellular materials can overcome the common weaknesses of truss/strut-based structures [17]. Additional information regarding the mechanical properties of TPMS structures is available in [17–22]. The design of TPMS structures for tissue scaffolds has attracted considerable attention in recent decades. Melchels et al. [23] demonstrated that the high permeability of the porous scaffold and robust accessibility of the pores lead to more biologically favorable behavior in cell proliferation and the transport of nutrients, and metabolites. Yoo [24,25] used a distance field to fabricate TPMS porous scaffolds for complex tissue models. Homogeneous porous scaffolds can be manufactured using this method; however, the manufacturing cost increases as the accuracy increases. Yang et al. [26] proposed a heuristic method for hybridizing different TPMS-based structures for bio-mimetic design. The combination of TPMS-based structures with different porous morphologies can be generated efficiently. Feng et al. [2] extracted the TPMS porous scaffolds from the solid T-spline designed volume. Natural bone demonstrates an anisotropic and heterogeneous material distribution, which requires tissue scaffold structures to satisfy these properties [26,27]. As described in [1,25], the internal tissue scaffolds of artificial skeletons must be composed of structures of different types and sizes continuously. The bio-morphic shape that best mimics the structural morphology would be a continuous surface, partitioned into multiple sub-spaces (pore and non-pore) [28]. Fig. 1 displays composite scaffolds with different sizes of TPMS-P (P surface) units. The different colors represent units with different sizes and porosities. The black boxes indicate progressively larger images of the multiporous scaffolds. As can be observed, nonuniform porosity and pore size can locally control the permeability and stiffness to satisfy the actual demand.

In this study, we focus on a composite porous scaffold design with complete consideration of the tissue engineering requirements and global architecture optimization based on TPMS properties. To the best of our knowledge, the proposed approach is the first algorithm to design a composite scaffold with multi-scale and multi-porosity triply periodic minimal structures with smooth merging between the different units. The proposed method can be divided into two steps. The first step is the novel merging algorithm with unit TPMS structures in the implicit function framework. The composite scaffold can be designed by merging different unit structures to satisfy the properties of internal connectivity. The second step is to optimize the designed composite scaffolds to satisfy the properties of TPMSs based on an operator splitting method. A modified Allen–Cahn type equation

with a correction term is proposed. The mean curvature on the surface is constant at all points in the equilibrium state. Typically, the obtained structure is smooth owing to the motion by mean curvature flow. Different numerical experiments are performed to demonstrate the efficiency and robustness of the proposed algorithm.

The remainder of this paper is organized as follows. Section 2 introduces the proposed methodology for composite scaffold design and optimization. Section 3 describes the numerical solution algorithm for the composite porous scaffold design. Several practical examples are presented in Section 4. Finally, concluding remarks and ideas for future research are presented in Section 5.

2. Description of the proposed method

In this section, we introduce a simple and efficient method for designing composite structures with TPMSs. The proposed method can be divided into two steps. First, we propose an efficient interpolation method for merginge different TPMS units in Section 2.1. Then, we modify the merged model to ensure the designed TPMS to satisfy the TPMS properties in Section 2.2.

2.1. Design of a composite structure with TPMS

A TPMS is a surface on which the curvature of each point is equal to a constant and has periodic boundary conditions [29–31]. TPMSs can be described implicitly, as indicated in Table 1.

To demonstrate the merging method clearly, we illustrate the process of merging two P surfaces in a two-dimensional (2D) domain. We divide the domain diagonally with a large P surface and two smaller P surfaces inserted. Let the 2D domain $\Omega = (0, L_x) \times (0, L_y)$ and $h = L_x/(N_x - 1) = L_y/(N_y - 1)$ be the uniform mesh size, where N_x and N_y are positive integers. Let $\psi_{i,j}$ be the approximation of $\psi((i - 1)h, (j - 1)h)$. In the finite difference method framework, we use the points of each cell center. Here, we know the points represented by circle ∘ and laid on diagonal lines (represented by dashed lines) as displayed in Fig. 2(a). We also know that the average value (represented by bullet •) of the right end of the larger P surface and left end of the smaller P surface. Our goal is to interpolate the two tiles naturally. Therefore, we first set the P surface in the domain and add a smaller P surface to the parts that represent the curve. We use the internal division between two points, represented by a circle and bullet, to determine the points indicated by ×. Points expressed by × should be redefined through linear interpolation. As can be observed in Fig. 2(b), the volume expressed in bullet × are interpolated. In the second step, we update the volume in the larger domain and find linear interpolation × in the smaller domain with average value • and points ∘, as indicated in Fig. 2(c). In the third step, we update the new volume in the smaller domain, as displayed in Fig. 2(d). This process functions in the same
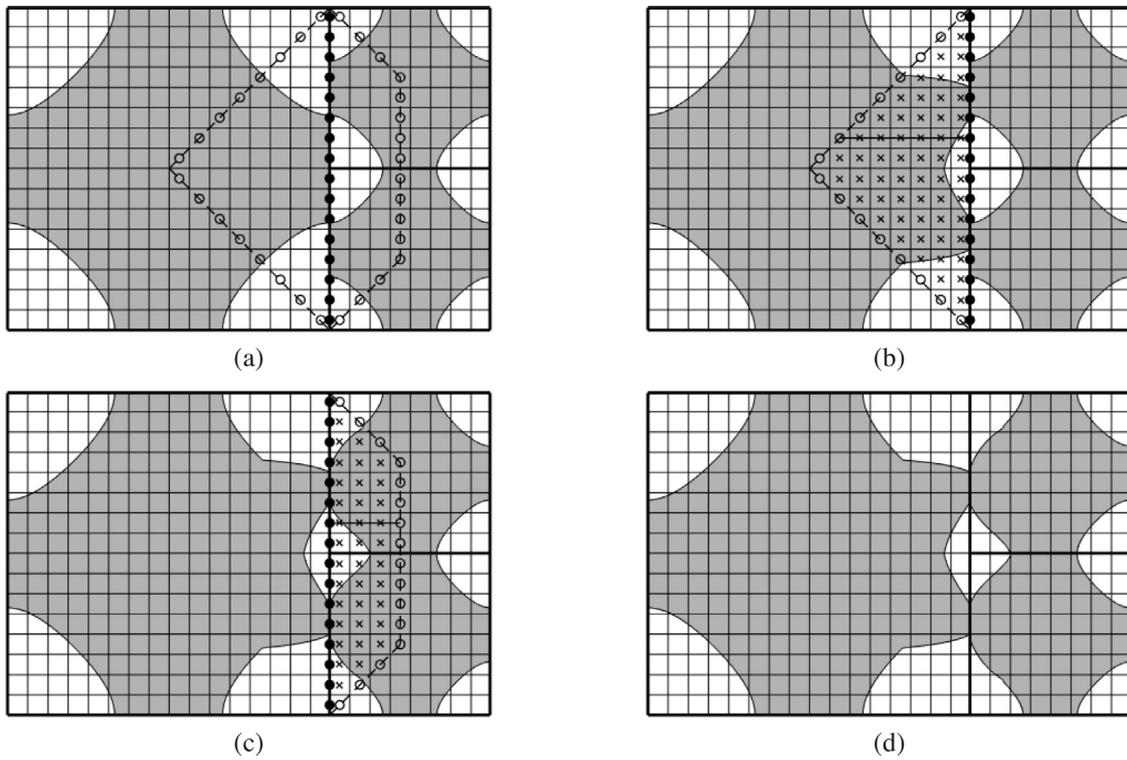
Fig. 2. Schematic of merging tiles in the 2D domain. (a) Before merging volume. (b) Interpolation indicated by × from two points represented by ○ and ● for the larger domain. (c) Interpolation indicated by × from two points represented by ○ and ● for the smaller domain. (d) After merging volume.

Table 1
Model demonstration and mathematical expression of TPMSs.

Type	Surface	Implicit equation
P		$\psi_P(x, y, z) = \cos(2\pi x) + \cos(2\pi y) + \cos(2\pi z) = 0$
D		$\psi_D(x, y, z) = \cos(2\pi x)\cos(2\pi y)\cos(2\pi z)$ $- \sin(2\pi x)\sin(2\pi y)\sin(2\pi z) = 0$
G		$\psi_G(x, y, z) = \sin(2\pi x)\cos(2\pi y)$ $+ \sin(2\pi z)\cos(2\pi x) + \sin(2\pi y)\cos(2\pi z) = 0$
I		$\psi_{I-WP}(x, y, z) = 2[\cos(2\pi x)\cos(2\pi y) + \cos(2\pi y)\cos(2\pi z)$ $+ \cos(2\pi z)\cos(2\pi x)] - \cos(4\pi x) - \cos(4\pi y) - \cos(4\pi z) = 0$

manner in a 3D domain. Figs. 3(a) and (b) illustrate the initial and final structure in a 3D domain, respectively. The schematic diagram in Fig. 3(b) describes the interpolation in a 3D domain.

In the level set framework, the calculated $\widetilde{\psi}$ uses the zero level as the interface to distinguish between the inside and the outside of the composite scaffold. The volume can be determined and denoted by a discrete function $\widetilde{\psi}(\mathbf{x})$, where $\widetilde{\psi}(\mathbf{x}) > 0$ if the voxel $\mathbf{x}$ is determined to be a volume voxel; otherwise, $\widetilde{\psi}(\mathbf{x}) < 0$. To link with Section 2.2, we define

$$\psi(\mathbf{x}) := \begin{cases} 1 & \text{if } \widetilde{\psi}(\mathbf{x}) > \alpha(\widetilde{\psi}_{max} - \widetilde{\psi}_{min}), \\ 0 & \text{if } \widetilde{\psi}(\mathbf{x}) < -\alpha(\widetilde{\psi}_{max} - \widetilde{\psi}_{min}), \\ \frac{0.5\widetilde{\psi}(\mathbf{x})}{\alpha(\widetilde{\psi}_{max} - \widetilde{\psi}_{min})} + 0.5 & \text{otherwise}, \end{cases}$$

where $\widetilde{\psi}_{max}$ and $\widetilde{\psi}_{min}$ are the maximum and minimum of $\widetilde{\psi}$, respectively. α is the hyperbolic tangent parameter that controls the conversion of the interfacial transition. Therefore, $\psi \in [0, 1]$ and the half level of ψ represent the surface of the volume, as indicated in Fig. 4.

2.2. Modification methodology for TPMS structures

Let us use $\phi(x)$ to define implicit surface $\Gamma = \{x : \phi(x) = 0.5\}$ in a 3D domain Ω, which implies that the interior of the surface is $\{x : \phi(x) > 0.5\}$ and the exterior of the surface is $\{x : \phi(x) < 0.5\}$. To ensure that the composite structure is a TPMS, i.e., $\kappa(\phi) = \lambda \ (\forall x \in \Gamma)$, we use the Allen–Cahn equation
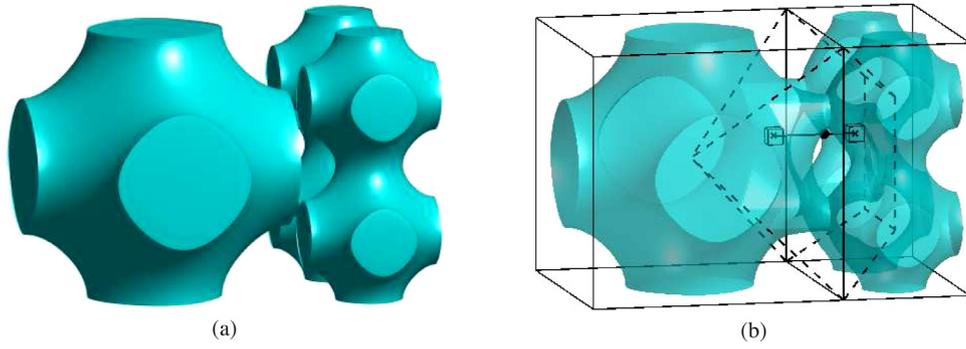
Fig. 3. Schematic of merging tiles in the 3D domain. (a) Before merging volume. (b) After merging volume.
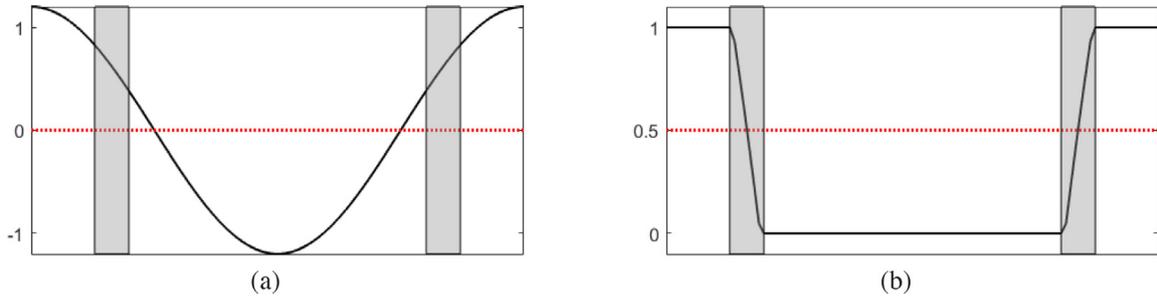
Fig. 4. (a) and (b) are the one-dimensional schematics of $\widetilde{\psi}$ and ψ, respectively. The gray region represents the interfacial region of the scaffold.

$\phi_t = |\nabla\phi|(\kappa(\phi) - \lambda(\phi))$ for the modification [32,33]. Here, κ is the mean curvature, and λ is the average value of the mean curvature over the surface, which can be denoted as

$$
\begin{cases}
\kappa = \nabla \cdot \left(\dfrac{\nabla\phi}{|\nabla\phi|} \right), \\
\lambda = \dfrac{\int_\Gamma \kappa \, ds}{\int_\Gamma ds} = \dfrac{\int_\Omega \kappa \delta(\phi) dx}{\int_\Omega \delta(\phi) dx},
\end{cases}
\tag{1}
$$

where $\delta(x)$ is the Dirac delta function. It should be conclusively confirmed that $\kappa(\phi) \equiv \lambda$ implies that the mean curvature on the surface is constant at all points. In our previous work [32], we combined the Cahn–Hilliard model with the variational level-set model and motivated the equilibrium profile

$$
F(\phi) = \frac{\phi^2(1-\phi)^2}{4} \approx \frac{\epsilon^2}{2}|\nabla\phi|^2.
\tag{2}
$$

Referring to [4], a hyperbolic tangent profile $\phi(x, t) = 0.5 + 0.5\tanh\big(d(x, t)/(2\sqrt{2}\epsilon)\big)$ is used in our phase field system, and we define $d(x, t)$ as the distance function, which is from the interface to x. The delta function of Eq. (1) is defined as $\delta(\phi) = |\nabla\phi|$ according to [34]. Based on the double-well potential functional in Eq. (2) and the regularized Dirac delta function, Eq. (1) can be derived as

$$
\kappa = \nabla\left(\frac{1}{|\nabla\phi|}\right) \cdot \nabla\phi + \frac{\Delta\phi}{|\nabla\phi|} = \nabla\left(\frac{\sqrt{2}\epsilon}{\phi(1-\phi)}\right) \cdot \nabla\phi + \frac{\Delta\phi}{|\nabla\phi|}
$$

$$
= -\frac{\sqrt{2}\epsilon(1-2\phi)|\nabla\phi|^2}{\phi^2(1-\phi)^2} + \frac{\Delta\phi}{|\nabla\phi|} = -\frac{(1-2\phi)}{\sqrt{2}\epsilon} + \frac{\sqrt{2}\epsilon\,\Delta\phi}{\phi(1-\phi)}
$$

$$
= \frac{\sqrt{2}}{\epsilon\phi(1-\phi)}\left(-\phi^3 + \frac{3}{2}\phi^2 - \frac{\phi}{2} + \epsilon^2\Delta\phi\right)
$$

$$
= \frac{1}{|\nabla\phi|}\left(-\frac{F'(\phi)}{\epsilon^2} + \Delta\phi\right)
\tag{3a}
$$

$$
\lambda = \frac{\int_\Omega \kappa\delta(\phi)dx}{\int_\Omega \delta(\phi)dx} = \frac{\int_\Omega \kappa|\nabla\phi|dx}{\int_\Omega |\nabla\phi|dx} = \frac{\sqrt{2}\int_\Omega \left(-F'(\phi) + \epsilon^2\Delta\phi\right)dx}{\epsilon\int_\Omega \phi(1-\phi)dx}
$$

$$
= \frac{-\sqrt{2}\int_\Omega F'(\phi)dx + \sqrt{2}\epsilon^2\int_{\partial\Omega}\frac{\partial\phi}{\partial n}d\mathbf{s}}{\epsilon\int_\Omega \phi(1-\phi)dx} = \frac{-\sqrt{2}\int_\Omega F'(\phi)dx}{\epsilon\int_\Omega \phi(1-\phi)dx}.
\tag{3b}
$$

Then, the modified Allen–Cahn can be rewritten as

$$
\phi_t = |\nabla\phi|(\kappa(\phi) - \lambda) = -\frac{F'(\phi)}{\epsilon^2} + \Delta\phi - \lambda\frac{\phi(1-\phi)}{\sqrt{2}\epsilon}.
\tag{4}
$$

By constructing the free energy functional in the L_2 space as

$$
\mathcal{E}(\phi) = \int_\Omega \left(\frac{F(\phi)}{\epsilon^2} + \frac{|\nabla\phi|^2}{2} + \lambda\frac{g(\phi)}{\sqrt{2}\epsilon}\right) d\mathbf{x} + \int_\Omega \frac{\beta}{2}(\psi(\mathbf{x}) - \phi(\mathbf{x}))^2 d\mathbf{x},
\tag{5}
$$

where $g(\phi) = \phi^2/2 - \phi^3/3$, we can derive the system with a constrained gradient flow as

$$
\begin{cases}
\dfrac{\partial\phi(\mathbf{x}, t)}{\partial t} = -\dfrac{F'(\phi(\mathbf{x}, t))}{\epsilon^2} + \Delta\phi(\mathbf{x}, t) - \lambda\dfrac{\phi(1-\phi)}{\sqrt{2}\epsilon} \\
\qquad + \beta(\psi(\mathbf{x}) - \phi(\mathbf{x}, t)), \quad \mathbf{x} \in \Omega, \ t > 0 \\
\phi(\mathbf{x}, 0) = \psi(\mathbf{x}), \quad \mathbf{x} \in \Omega, \\
\dfrac{\partial\phi(\mathbf{x}, t)}{\partial\mathbf{n}} = 0, \quad \mathbf{x} \in \partial\Omega, \ t > 0,
\end{cases}
\tag{6}
$$

Here, β is a positive constant, ϕ satisfies the Neumann boundary conditions on $\partial\Omega$, and $\mathbf{n}$ is the outward normal vector. As mentioned in Section 2.1, ψ describes a merged structure from two nearby TPMSs; it approximates but is not a minimal surface. The obtained discrete function $\phi(x)$, which approaches the given $\psi(x)$, indicates that the curvature of each point on the surface is equal to a constant. This system can ensure that the calculated
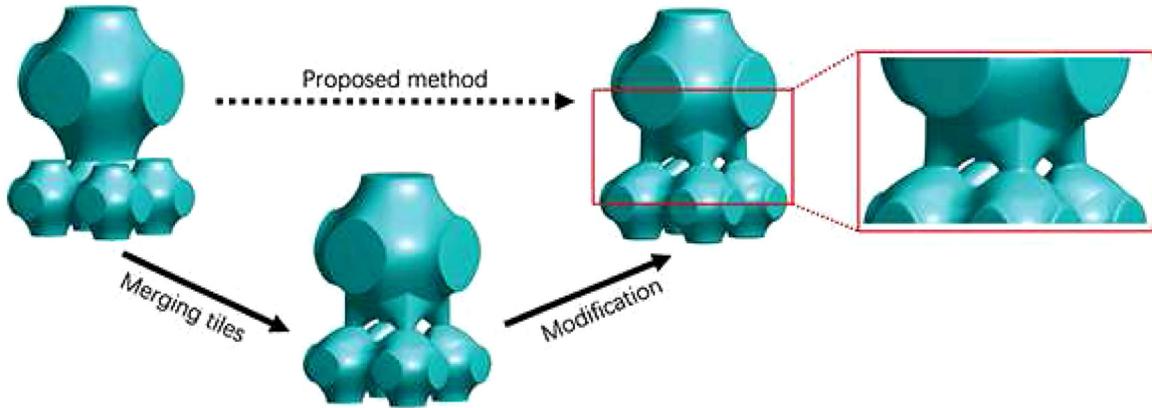
Fig. 5. Flowchart of the framework for the volume merging method.

results, ϕ, remain as similar as possible to the original model, ψ. The modified Allen–Cahn equation (6) ensures that total energy $\mathcal{E}(\phi)$ in Eq. (5) decreases with time:

$$\frac{d}{dt}\mathcal{E}(\phi) = \int_{\Omega}\left(\frac{F'(\phi)}{\varepsilon^2}\phi_t + \nabla\phi\cdot\nabla\phi_t + \lambda\frac{g'(\phi)}{\sqrt{2}\epsilon}\phi_t\right)d\mathbf{x}$$

$$- \beta\int_{\Omega}(\psi-\phi)\phi_t d\mathbf{x}$$

$$= \int_{\Omega}\left(\frac{F'(\phi(\mathbf{x},t))}{\varepsilon^2} - \Delta\phi(\mathbf{x},t) + \lambda\frac{\phi(1-\phi)}{\sqrt{2}\epsilon}\right. \tag{7}$$

$$\left. - \beta(\psi(\mathbf{x})-\phi(\mathbf{x},t))\right)\phi_t d\mathbf{x} = -\int_{\Omega}\phi_t^2 d\mathbf{x} \leq 0,$$

which implies that the solution of Eq. (6) is stable. Observing the modified equation, we find that function ϕ becomes a minimal structure in the equilibrium condition. The overall shape is similar to the original ψ because of fidelity term $\beta(\psi-\phi)$. Therefore, the structure of the merged tiles can be modified as a minimal surface. In summary, the flowchart of the framework for improving the merged volume is displayed in Fig. 5.

3. Numerical solution

We employ a fast scheme with an operator splitting-based hybrid numerical method to obtain an efficient scheme. Let $N_x \times N_y \times N_z$ be the number of voxels in the computational domain, where N_x, N_y, and N_z are even integers. Let $x_i = ih_x$, $y_j = jh_y$, $z_k = kh_z$, $1 \leq i \leq N_x$, $1 \leq j \leq N_y$, and $1 \leq k \leq N_z$, where h_x, h_y, and h_z are the uniform mesh sizes. Furthermore, we define ϕ_{ijk}^n as an approximation of $\phi(\mathbf{x}_{ijk}, n\Delta t)$, where $\mathbf{x}_{ijk} = (x_i, y_j, z_k)$ and Δt is the time step. Considering the original problem in Eq. (6), we refer to our previous work [33] and divide it into a series of simpler problems as

$$\frac{\partial}{\partial t}\phi^1(\mathbf{x},t) = \beta(\psi(\mathbf{x})-\phi^1(\mathbf{x},t)), \quad (n-1)\Delta t < t \leq n\Delta t, \tag{8a}$$

$$\frac{\partial}{\partial t}\phi^2(\mathbf{x},t) = \Delta\phi^2(\mathbf{x},t) + \frac{\lambda\phi^1(1-\phi^1)}{\sqrt{2}\epsilon}, \quad (n-1)\Delta t < t \leq n\Delta t, \tag{8b}$$

$$\frac{\partial}{\partial t}\phi^3(\mathbf{x},t) = -\frac{F'(\phi^3)}{\epsilon^2}, \quad (n-1)\Delta t < t \leq n\Delta t. \tag{8c}$$

Here, we use ϕ^1, ϕ^2, and ϕ^3 to denote the solutions of Eqs. ((8)a), ((8)b) and ((8)c) as

$$\begin{cases} \phi^1(\mathbf{x},(n-1)\Delta t) = \phi(\mathbf{x},(n-1)\Delta t), \\ \phi^2(\mathbf{x},(n-1)\Delta t) = \phi^1(\mathbf{x},n\Delta t), \\ \phi^3(\mathbf{x},(n-1)\Delta t) = \phi^2(\mathbf{x},n\Delta t). \end{cases} \tag{9}$$

The solution of Eq. (6) at time $t = n\Delta t$ is $\phi(\mathbf{x},n\Delta t) = \phi^3(\mathbf{x},n\Delta t)$. Eq. ((8)a) is an ordinary differential equation, i.e. $\beta dt + \frac{1}{\phi-\psi}d\phi = 0$. With initial condition ϕ_{ijk}^n, we obtain the following solution after Δt:

$$\phi_{ijk}^{1,n+1} = e^{-\beta\Delta t}\phi_{ijk}^n + (1-e^{-\beta\Delta t})\psi_{ijk}. \tag{10}$$

We demonstrate an implicit method based on the result of the previous subproblem as

$$\frac{\phi_{ijk}^{2,n+1} - \phi_{ijk}^{1,n+1}}{\Delta t} = \Delta\phi_{ijk}^{2,n+1} + \frac{\lambda\phi_{ijk}^{1,n+1}(1-\phi_{ijk}^{1,n+1})}{\sqrt{2}\epsilon}, \tag{11}$$

which can be solved using a GPU-accelerated discrete cosine transform (DCT) solver. Based on Eq. (3b), λ is computed as

$$\lambda = \frac{-\sqrt{2}\sum_{i=1}^{N_x}\sum_{j=1}^{N_y}\sum_{k=1}^{N_z}F'(\phi_{ijk}^{1,n+1})}{\epsilon\sum_{i=1}^{N_x}\sum_{j=1}^{N_y}\sum_{k=1}^{N_z}\phi_{ijk}^{1,n+1}(1-\phi_{ijk}^{1,n+1})}. \tag{12}$$

Here, the homogeneous Neumann volume condition is applied. We rewrite Eq. ((8)c) as

$$0 = \frac{dt}{\epsilon^2} + \frac{d\phi}{F'(\phi)} = \frac{dt}{\epsilon^2} + \frac{-2d\phi}{\phi} + \frac{4d\phi}{\phi-0.5} + \frac{2d\phi}{1-\phi}, \tag{13}$$

and then solve this as

$$\phi_{ijk}^{n+1} = \phi_{ijk}^{3,n+1} = \frac{1}{2} + \frac{\phi_{ijk}^{2,n+1} - 0.5}{\sqrt{e^{\frac{-\Delta t}{2\epsilon^2}} + (2\phi_{ijk}^{2,n+1}-1)^2(1-e^{\frac{-\Delta t}{2\epsilon^2}})}}, \tag{14}$$

with initial condition $\phi_{ijk}^{2,n+1}$.

To confirm that the total energy is globally non-increasing, we must prove that $\epsilon(\phi^{n+1}) \leq \epsilon(\phi^n)$. The proposed discrete scheme is not unconditionally energy stable owing to nonlinear term $\lambda\phi(1-\phi)/(\sqrt{2}\epsilon)$. However, the numerical tests in Section 4.1 indicate that the numerical scheme is stable with an appropriate time step. The proposed governing equation (6) can be solved using other energy stable schemes, such as the convex splitting temporal [35], operator splitting coupled with the Fourier pseudo-spectral approximation [36], and backward differentiation formula numerical schemes [37]. The energy stability
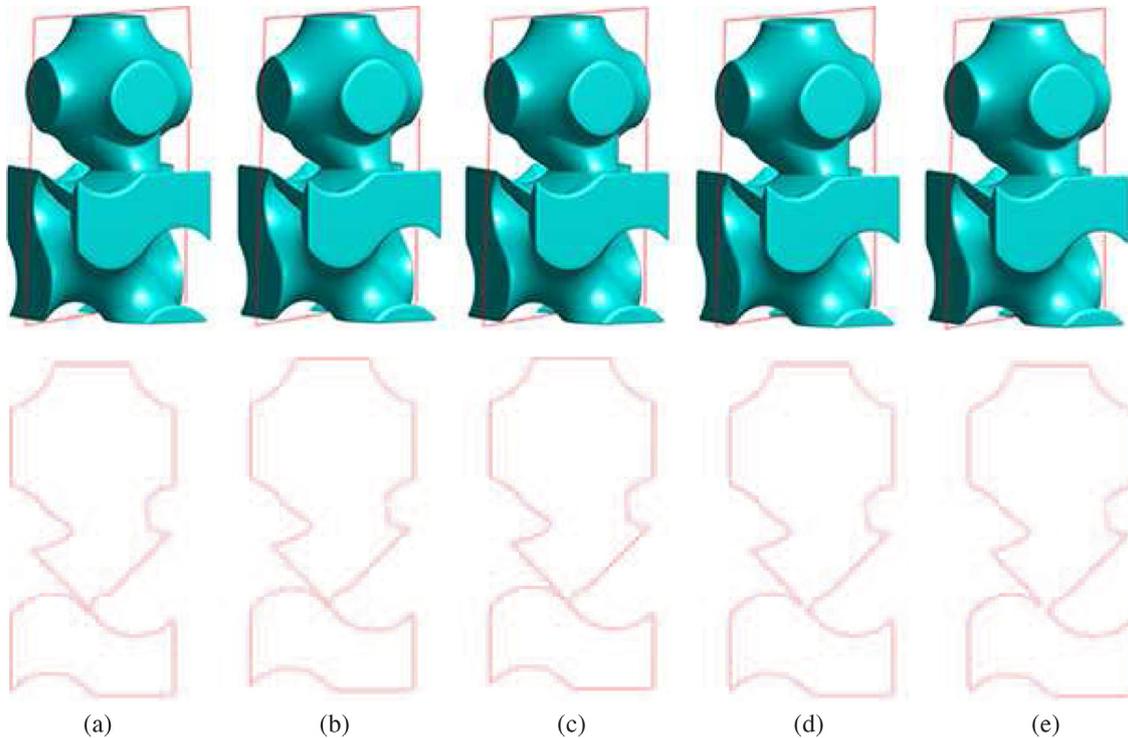
Fig. 6. Evolution of the 3D volume (top row) and 2D contours (bottom row). The porous scaffold is composed of P-surface and G-surface unit structures. The red line denotes the 0.5 level of the middle slice of the composite scaffold. From (a) to (e), the iterations are 1, 4, 8, 12, and 18, respectively.
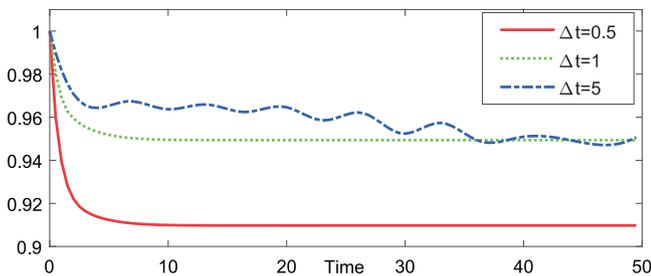
Fig. 7. Evolution of total energy of the proposed model for three time steps. It should be noted that we have normalized the total energy by the energy at the initial time.

and convergence analysis of the operator splitting method can be found in [36,38]. There are also different numerical schemes in Eq. (6), such as the energy stable SAV-type [39], high order exponential time [40,41], and modified energy stable BDF2 schemes [42]. Compared to the aforementioned schemes, the advantages of the proposed scheme are summarized as follows. (i) The proposed numerical method for Eqs. (10), (11), and (14) is easy to implement and can achieve fast convergence as the algorithm consists of two analytical evaluations for the ordinary differential equations and one implicit Poisson-type equation solver. (ii) For ordinary differential equations, their computational complexity is $O(N)$, where N is the size of the mesh grid. For the implicit Poisson-type equation solver, we apply a fast DCT method with a computational complexity of $O(N \log N)$. (iii) The proposed numerical scheme can be applied in a straightforward manner to a GPU-accelerated DCT implementation, which can be executed multiple times faster than CPU-only alternatives.

4. Experimental tests

In this section, we focus on the continuous connection between different unit scaffolds in biological tissue and obtaining

superior mechanical properties of the structure. We will discuss different types of scaffolds based on TPMSs. We stop the evolution and regard the numerical results as the steady-state solution when relative error $\|\phi^{n+1} - \phi^n\|_2 / \|\phi^n\|_2$ is less than a tolerance *tol*. Unless otherwise stated, throughout this paper, we use $h = 1$, $\Delta t = 0.5$, and $\epsilon = 1$.

4.1. Evolution of our proposed algorithm

Fig. 6 displays the evolution of the proposed modified algorithm. Here, we use a composite scaffold consisting of P-surface and G-surface unit structures. In Fig. 6(a) to (e), the iterations are 1, 4, 8, 12, and 18, respectively. The tolerance is $tol = 1e{-}4$. Fidelity term parameter β is set to 0.3. As can be observed, the surface of the composite structure becomes smooth under the influence of the mean curvature flow. To illustrate the details, we display the 0.5 level of the middle slice. The internal region is gradually connected under the mean curvature flow.

To demonstrate the energy dissipation with the composite structure, we plot the discrete total energy curves with three different time steps: $\Delta t = 0.5$, $\Delta t = 1$, and $\Delta t = 5$ in Fig. 7. It should be noted that we have normalized the total energy by the total energy at the initial time. As can be observed in Fig. 7, the discrete total energy is non-increasing. The time step is less than 1, i.e., $\Delta t \leq 1$. The discrete total energy curve is unstable when a larger time step is used. However, it is well known that large time steps can cause less accurate results, and smaller time steps result in greater computational costs. Therefore, to maintain the proposed scheme's accuracy and reduce computational costs, an appropriate value for Δt is 0.5.

Fig. 8 displays the evolution of the average mean curvature. As expected for the mean curvature flow, the solid red line gradually converges to the dotted blue line after undulating, which means that the average mean curvature of the composite scaffold gradually converges to a fixed value and implies that the surface of the composite scaffold has constant mean curvature.
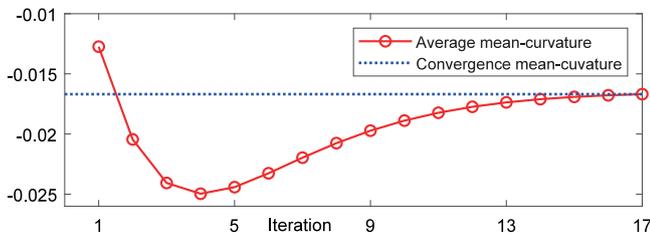
Fig. 8. Evolution of the average mean curvature with iterative steps. The dotted blue line represents the converged mean curvature.

4.2. Scaffold with different sizes of TPMSs

There is a demand for merging scaffolds of different sizes in an artificial tissue scheme [43]. In the artificial tissue model, the boundary and the inner regions require different precision for the scaffolds [14]. However, in the process of merging structures of different sizes, problems such as disconnectedness and the dissatisfying properties of minimal surfaces become challenges in the application of a composite scaffold for biological tissue models as indicated in the left subfigure in Fig. 9.

The right subfigure in Fig. 9 displays the composite scaffold obtained using the proposed method. For more internal details, we selected eight consecutive slices of the connecting region in the middle of the scaffold for display. From the gray figures, we can observe the contrast changes in the composite scaffold. It is important to note that the proposed method can effectively design a multi-scale tissue scaffold and maintain its internal connectivity.

To demonstrate that the designed composite scaffold can be manufactured correctly using additive manufacturing techniques, we manufactured a multi-scale P-surface scaffold, as shown in Fig. 10. It can be observed that the composite scaffold is suitable for manufacturing, with acceptable stability and strong connectivity. Furthermore, it can be printed without support structures. In particular, this property of printing without support structures is extremely important in the 3D printing of bio-related scaffolds.

To demonstrate the efficiency of the composite porous scaffold obtained using the proposed method, we computed the magnitude and distribution of the von Mises stress on a loading force of 150 N using the finite element method. Here, the material of the Schwarz P unit cells is assumed to be homogeneous, isotropic, and linearly elastic poly-DL-lactide. Fig. 11(a) and (b) show the magnitude and distribution of the von Mises stress on the modified and original scaffolds, respectively. The simulation results confirm that the stresses on the modified scaffold are more smoothly distributed than those on the original scaffold. These results imply that the modified scaffold structure is more stable than the original.
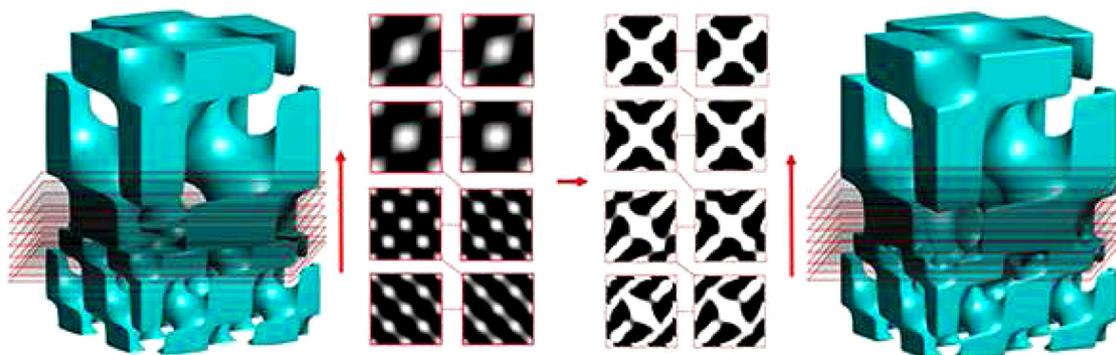
4.3. Scaffold with different porosities of TPMS

For cell growth and the adhesion of biological tissue, scaffolds should have many pores. The highly porous structure should have a large surface area for cell growth and sufficient volume for blood vessel growth [43–45]. In addition, the size of the pores and specification of the porosity influence the mechanical stability [46]. In the field of tissue engineering, porous scaffolds with non-uniform properties are desired. Salgado et al. [47] proposed that the bone tissue varies spatially in terms of structure and composition, and different bone tissues have different characteristics to address the different requirements. Structures with acceptable performance for tissue or cell culturing make a significant difference in tissue engineering [48]. Hence, tissue scaffolds that have property gradients such as porosity and permeability are desirable. With the proposed method, continuous variation between the TPMS unit scaffolds with different porosities can be easily generated, as shown in Fig. 12. Here, $\beta = 0.5$ and $tol = 1e-4$ are used. To better demonstrate the superiority of the proposed algorithm better, we combined eight P-surface structures with different porosities in the composite scaffold. In addition, we demonstrate the composite structures from different perspective, and slice the scaffold uniformly along the z-direction, as shown in the top row of Fig. 12. As can be seen, the proposed method can achieve continuous transition between the unit structures and retain the main characteristics of the TPMS. Furthermore, the developed program successfully generated defect-free human bone scaffolds for TPMS-based unit cell libraries. For example, we used P-surface unit scaffolds to design the skeleton model internally, as shown in Fig. 1. With this method, the internal regions of the scaffold are properly combined with the given shapes of the bone models in a conforming manner by the signed distance field with the arbitrarily shaped bone models. Observing the numerical results, the proposed method can effectively design different porous scaffolds with high-quality external anatomical bone surfaces.

4.4. Parameter sensitivity analysis

We conducted a parameter sensitivity analysis for model parameters tol and β. The last term in Eq. (6) is the fidelity term to ensure that ϕ remains close to ψ. Parameter β balances the fidelity term and motion by mean curvature flow, which means that it can control the convergent mean curvature of the structure. As can be seen in Fig. 13, different β values can lead to different results. From Fig. 13(a) to (d), we choose β as 0.01, 0.1, 1, and 10, respectively, leading to mean curvatures of 0.022, -0.012, -0.05, and -0.032, respectively. To demonstrate the influence of β further, we plotted 0.5 contour lines in Fig. 13(e).

Fig. 9. Composite structure with the D-surface. The size of the structure above is twice that of the structure below. The grayscale images are eight slices at the connection area of the composite structure.
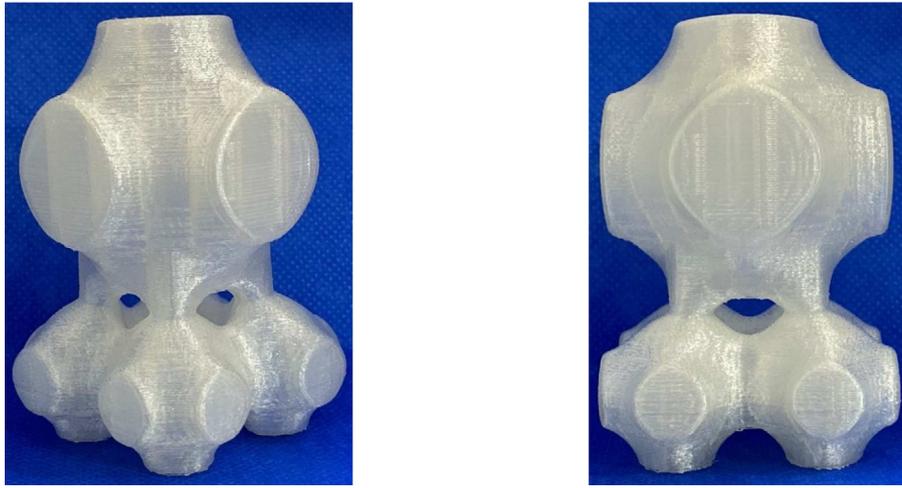
Fig. 10. Physical model manufactured from the proposed mathematical algorithm in different views.
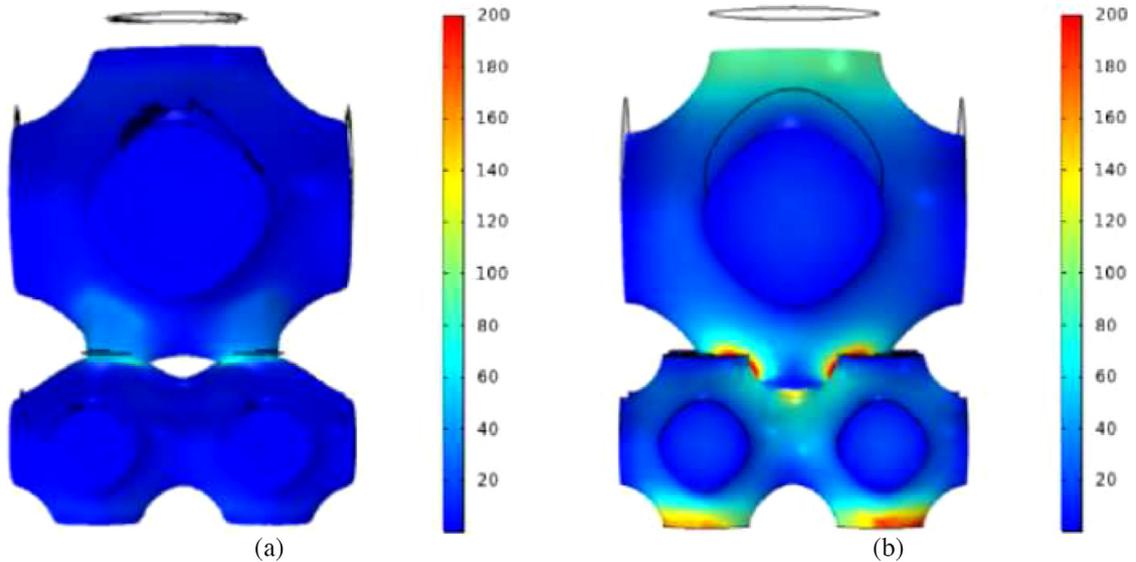
Fig. 11. Von Mises stress distribution. (a) Modified scaffold. (b) Original scaffold. The two structures are verified to have identical loading conditions and material properties.

Table 2
Effect of *tol* values.

Tolerance	Iteration	Average mean curvature	CPU time (s)
$1e{-}1$	1	-0.024	0.73
$1e{-}4$	15	-0.038	9.98
$1e{-}8$	53	-0.038	36.52

Here, the red, green, blue, and magenta colors represent isolines with β values of 0.01, 0.1, 1, and 10, respectively. From the close-up view, we can see that the surface of the composite scaffold is smoother with smaller values of β. Therefore, considering algorithm efficiency, we suggest using $0.1 \le \beta \le 1$.

Eq. (6) ensures that the total energy, $\mathcal{E}(\phi)$, decreases with respect to time, which implies that the solution of the proposed method is stable. Therefore, we can stop the evolution and assume that the computational result is a steady-state solution when relative error $\|\phi^{n+1} - \phi^n\|_2 / \|\phi^n\|_2$ is less than tolerance *tol*. Here, we choose $tol = 1e{-}1$, $tol = 1e{-}4$, and $tol = 1e{-}8$. As shown in Fig. 14, the volume obtained using $tol = 1e{-}8$ appears to be marginally smoother than that using $tol = 1e{-}4$. Observing

the results in Table 2, a smaller *tol* requires considerably more iterations to achieve a relative error for the numerical solution that is less than the given *tol*. An acceptable stopping condition is important for the efficiency of the proposed partial differential equation-based method. In this paper, we suggest using $tol = 1e{-}4$.

4.5. Design of a porous scaffold with a simple external shape

In this section, we use the distance field method for Boolean operations between the composite scaffold and external surface. Let us define ϕ_s and ϕ_{cs} as the implicit functions of the external surface and composite scaffold, respectively. Boolean operations such as union, subtraction, and intersection can be defined as follows:

$$\begin{cases} \phi_s \cup \phi_{cs} = \max(\phi_s, \phi_{cs}) \ \text{(union)} \\ \phi_s - \phi_{cs} = \min(\phi_s, -\phi_{cs}) \ \text{(subtraction)} \\ \phi_s \cap \phi_{cs} = \min(\phi_s, \phi_{cs}) \ \text{(intersection)} \end{cases}$$

Using these methods, we can avoid the time-consuming trimming and re-meshing operations. To illustrate this method further, we
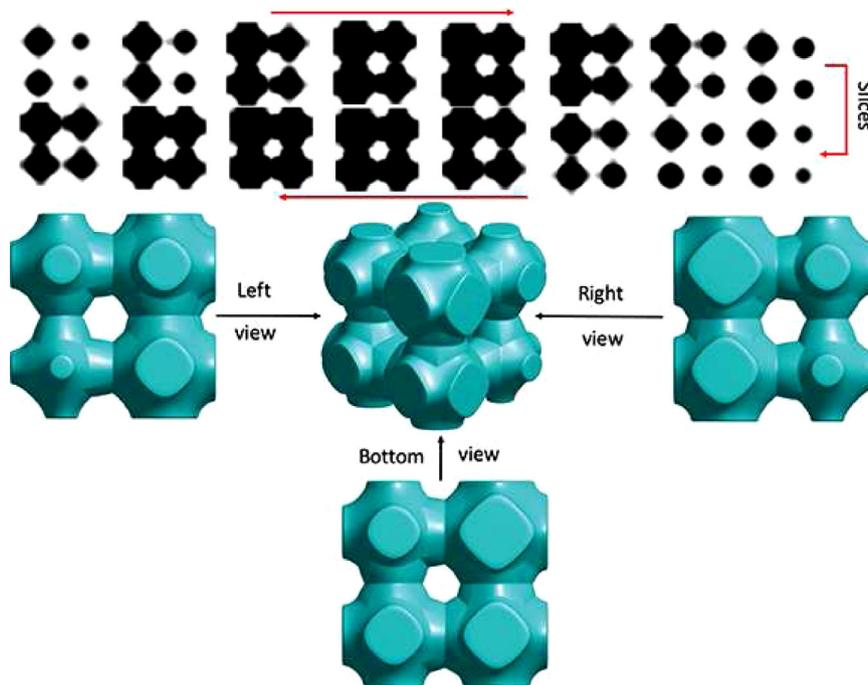
Fig. 12. Combination of multi-porosity P-surface. The top row presents the internal slices along the z-direction. The bottom row shows the three directional views.
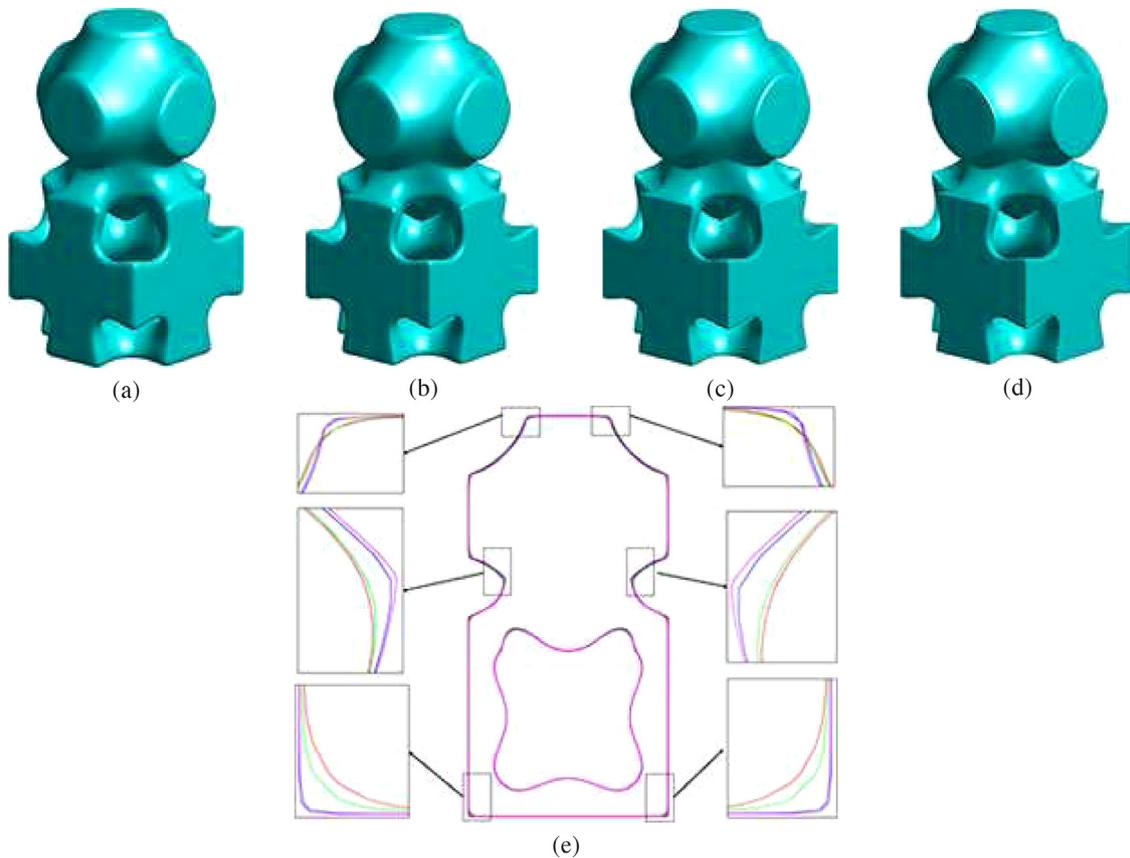
Fig. 13. Parameter sensitivity analysis for β in fidelity term. The complex scaffold is composed of a P-surface and I-WP-surface unit structures. From (a) to (d), β is 0.01, 0.1, 1, and 10, respectively. Stop condition *tol* is the same for the four results as in $1e-4$. (e) 0.5 contour lines of slices from (a) to (d). Red, green, blue, and magenta represent lines with β of 0.01, 0.1, 1, and 10, respectively. (For interpretation of the references to color in this figure legend, the reader is referred to the web version of this article.)

demonstrate a cylinder composed of a multi-scale P-surface as shown in Fig. 15. Fig. 15(a) shows a porous scaffold with a unit

P-surface with the same scale, where the solid red line is the unit circle. Then, we replace the original scaffold with the P-surface
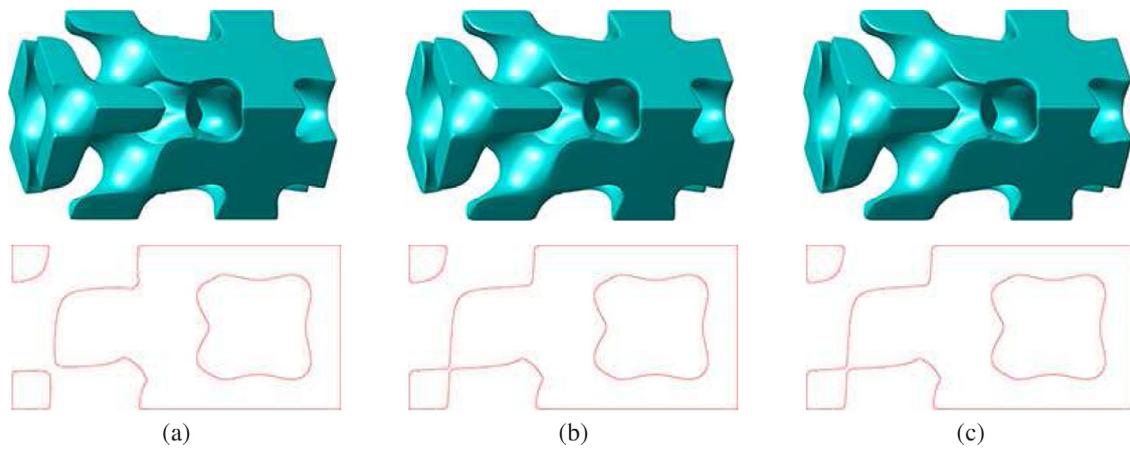
Fig. 14. Parameter sensitivity analysis for stop condition *tol*. The top row is the 3D scaffold surface. The bottom row is the 0.5 contour of the middle slice. From (a) to (c), tolerance $tol = 1e-1$, $1e-4$ and $1e-8$, respectively. β is fixed at 0.5.
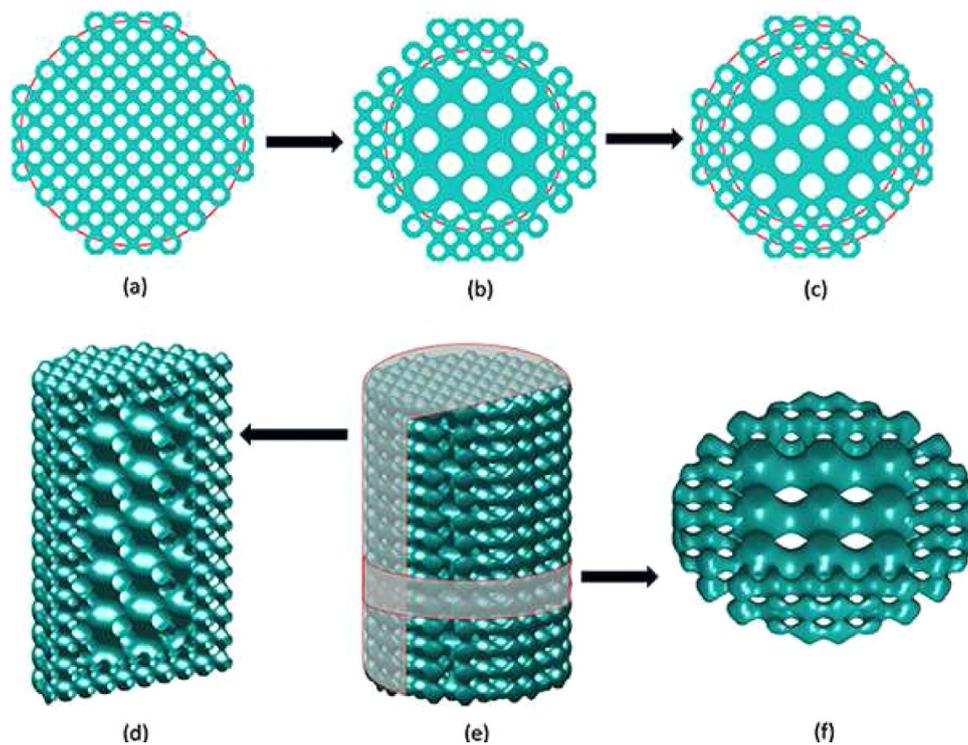
Fig. 15. Hollow cylinder composite scaffold with a multi-scale P-surface micro-structure. The top and bottom rows represent the simulation results of a composite scaffold in the 2D and 3D domains, respectively. (d) and (f) are the portrait and landscape closer view of (e), respectively.

of a scale that is twice as large in a circle of 0.8, as displayed in Fig. 15(b). It can be observed that there is no acceptable transition or connection between the structures of different scales. With the proposed method, the multi-scale composite scaffold becomes strongly connected, as shown in Fig. 15(c). In the 3D space, we used the cylinder surface and composite scaffold to perform the Boolean operation, as shown in Fig. 15(e). Fig. 15(d) and (f) are portrait and landscape closer views of (e), respectively. It is important to note that the proposed method can be effectively combined with the signed distance field to construct a composite scaffold with a complex anatomical external shape.

4.6. Application of composite scaffolds

To verify the efficiency of the proposed method in designing an actual bone model, we implement subarea fabrication with different unit sizes and porosities. Fig. 16(a) shows a segmented human bone from a CT image. Fig. 16(b) shows the fabricated scaffold with non-uniform G-surface units. Fig. 16(c) is a closer view of Fig. 16(b). The proposed method can achieve a hierarchical design for tissue engineering.

The signed distance field is used to fabricate the bone tissue with P surface unit successfully. Fig. 17 shows a visualization of the resulting scaffold. For improved visualization, we show the brittle part of the bone. Fig. 17(a) shows the three level contours of the signed distance function. We fabricated a scaffold with different porosities with P structure units in the areas of different colors, as indicated in Fig. 17(b). The blue, cyan, and red colors represent structures with porosities of 50%, 70%, and 90%, respectively. It is clear that the pore size of the scaffold close to the boundary is considerably smaller than that at the middle, where the gradient changes in pore size and porosity are distinct. Comparing this result with the conventionally designed porous
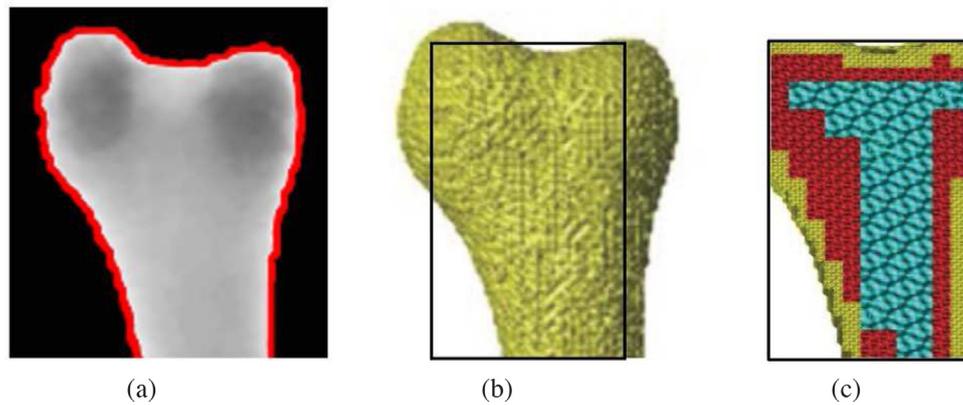
Fig. 16. (a) Segmented human bone from a CT image. (b) Adaptive fabricated scaffold with non-uniform G-surface units. (c) Closer view of (b).
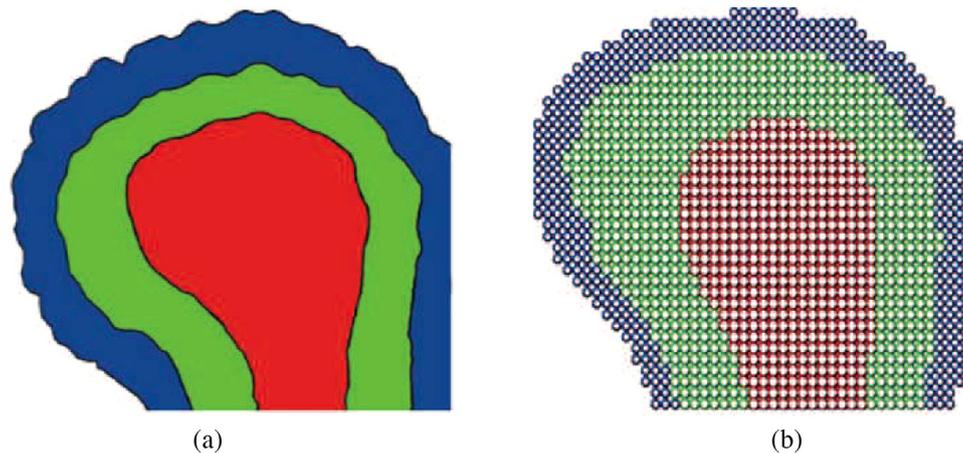
Fig. 17. Scaffold fabrication with variable porosity in the head of the arm bone. (a) Divided regions for different porosities. (b) Designed scaffold with multi-porosity. (For interpretation of the references to color in this figure legend, the reader is referred to the web version of this article.)

scaffold, we can observe that the proposed method decreases the porosity naturally from the middle of the bone structure downwards. This non-uniform distribution in porosity and pore size can change the permeability and stiffness to adapt to actual demands.

5. Conclusion

The main objective of this study was to design composite porous scaffolds for tissue engineering. First, we proposed a novel merging algorithm for composite porous scaffolds using a unit TPMS and an implicit function framework. To the best of our knowledge, this is the first attempt to design multi-scale composite porous scaffolds using the finite difference method. Then, we optimized the designed composite scaffolds based on an Allen–Cahn type equation to satisfy the properties of the TPMSs. Based on the operator splitting method, the proposed algorithm consists of two analytical evaluations for the ordinary differential equations and one implicit Poisson-type equation solver. The proposed numerical scheme can straightforwardly be applied to a GPU-accelerated DCT implementation, which can be executed multiple times faster than CPU-only alternatives. The optimized scaffold has a smooth surface, where the mean curvature of each point is constant owing to the motion by mean curvature flow. Several numerical examples were presented to demonstrate that the proposed method is robust and produces multi-scale composite scaffolds with superior performance.

Declaration of competing interest

The authors declare that they have no known competing financial interests or personal relationships that could have appeared to influence the work reported in this paper.

References

[1] D.W. Hutmacher, Biomaterials 21 (2000) 2529–2543.
[2] J. Feng, J. Fu, C. Shang, Z. Lin, B. Li, Comput. Methods Appl. Mech. Engrg. 336 (2018) 333–352.
[3] Y. Wang, Comput. Aided Des. 39 (2007) 179–189.
[4] S.D. Yang, H.G. Lee, J. Kim, Commun. Comput. Phys. 181 (2010) 1037–1046.
[5] T.S. Huang, M.N. Rahaman, N.D. Doiphode, M.C. Leu, B.S. Bal, D.E. Day, X. Liu, Mater. Sci. Eng. C 31 (2011) 1482–1489.

[6] X.Y. Kou, S.T. Tan, Comput. Aided Des. 42 (2010) 930–941.

[7] P. Geoffroy-Donders, G. Allaire, O. Pantz, J. Comput. Phys. 401 (2020) 108994.

[8] C.K. Chua, K.F. Leong, C.M. Cheah, S.W. Chua, Int. J. Adv. Manuf. Technol. 21 (2003) 291–301.

[9] M.W. Naing, C.K. Chua, K.F. Leong, Y. Wang, Rapid Prototyping J. 11 (2005) 249–259.

[10] D. Puppi, C. Mota, M. Gazzarri, D. Dinucci, A. Gloria, M. Myrzabekova, L. Ambrosio, F. Chiellini, Biomed. Microdevices. 14 (6) (2012) 1115–1127.

[11] S.J. Hollister, R.A. Levy, T.M. Chu, J.W. Halloran, S.E. Feinberg, Int. J. Oral Maxillofac. Surg. 29 (2000) 67–71.

[12] Y.M. Xie, G.P. Steven, Basic Evolutionary Structural Optimization, Springer, 1997.

[13] J.A. Sanz-Herrera, J.M. García-Aznar, M. Doblaré, Comput. Methods Appl. Mech. Engrg. 197 (2008) 3092–3107.

[14] S. Rajagopalan, R.A. Robb, Med. Image Anal. 10 (2006) 693–712.

[15] S. Gómez, M.D. Vlad, J. López, E. Fernández, Acta Biomater. 42 (2016) 341–350.

[16] F. Liu, Z. Mao, P. Zhang, D.Z. Zhang, J. Jiang, Z. Ma, Mater. Des. 160 (2018) 849–860.

[17] D.W. Abueidda, M. Bakir, Rashid K. Abu Al-Rub, J.S. Bergstrom, N.A. Sobh, I. Jasiuk, Mater. Des. 122 (2017) 255–267.

[18] J.R. Jones, G. Poologasundarampillai, R.C. Atwood, D. Bernard, P.D. Lee, Biomaterials 28 (2007) 1404–1413.

[19] A.L. Olivares, E. Marsal, J.A. Planell, D. Lacroix, Biomaterials 30 (2009) 6142–6149.

[20] Y. He, Y. Zhou, Z. Liu, K.M. Liew, Mater. Des. 132 (2017) 375–384.

[21] O. Al-Ketan, R.K.A. Al-Rub, Adv. Eng. Mater. 21 (2019) 1900524.

[22] L. Zhang, S. Feih, S. Daynes, S. Chang, M.Y. Wang, J. Wei, W.F. Lu, Addit. Manuf. 23 (2018) 505–515.

[23] F.P.W. Melchels, A.M.C. Barradas, C.A.V. Blitterswijk, J.D. Boer, J. Feijen, D.W. Grijpma, Acta. Biomater. 6 (2010) 4208–4217.

[24] D.J. Yoo, Int. J. Precis. Eng. Man. 12 (2011) 61–71.

[25] D.J. Yoo, Biomaterials 32 (2010) 7741–7754.

[26] N. Yang, Z. Quan, D. Zhang, Y. Tian, Comput. Aided Des. 56 (2014) 11–21.

[27] S.J. Hollister, C.Y. Lin, Comput. Methods Appl. Mech. Engrg. 196 (2007) 2991–2998.

[28] S.C. Kapfer, S.T. Hyde, K. Mecke, C.H. Arns, G.E. Schröder-Turk, Biomaterials 32 (2011) 6875–6882.

[29] J.K. Guest, J.H. Prévostb, Comput. Methods Appl. Mech. Engrg. 196 (2007) 1006–1017.

[30] X.C. Ye, X.C. Lin, J.Y. Xiong, H.H. Wu, G.W. Zhao, D. Fang, Mater. Res. Express. 6 (2019) 125609.

[31] Y. Jung, K.T. Chu, S. Torquato, J. Comput. Phys. 223 (2007) 711–730.

[32] Y. Li, S. Guo, Appl. Math. Comput. 295 (2017) 84–94.

[33] Y. Li, S. Lan, X. Liu, B. Lu, L. Wang, Pattern Recognit. 107 (2020) 107478.

[34] H.G. Lee, J. Kim, Internat. J. Numer. Methods Engrg. 91 (2012) 269–288.

[35] J. Shen, C. Wang, X. Wang, S.M. Wise, SIAM J. Numer. Anal. 50 (2012) 105–125.

[36] C. Zhang, H. Wang, J. Huang, C. Wang, X. Yue, Appl. Numer. Math. 119 (2017) 179–193.

[37] Y. Yan, W. Chen, C. Wang, S.M. Wise, Commun. Comput. Phys. 23 (2018) 572–602.

[38] X. Li, Z. Qiao, H. Zhang, SIAM J. Numer. Anal. 55 (2017) 265–285.

[39] C. Zhang, J. Ouyang, C. Wang, S.M. Wise, J. Comput. Phys. 423 (2020) 109772.

[40] K. Cheng, Z. Qiao, C. Wang, J. Sci. Comput. 81 (2019) 154–185.

[41] Y. Li, H.G. Lee, B. Xia, J. Kim, Comput. Phys. Commun. 200 (2016) 108–116.

[42] W. Chen, C. Wang, S. Wang, X. Wang, S.M. Wise, J. Sci. Comput. 84 (2020) 27.

[43] X.H. Liu, P.X. Ma, Ann. Biomed. Eng. 32 (2004) 477–486.

[44] S.J. Hollister, Nature Mater. 4 (2005) 518–524.

[45] Z. Dong, Y. Li, Q. Zou, Appl. Surf. Sci. 255 (2009) 6087–6091.

[46] F. Yang, R. Murugan, S. Ramakrishna, X. Wang, Y.X. Ma, S. Wang, Biomaterials 25 (2004) 1891–1900.

[47] A.J. Salgado, O.P. Cotinho, R.L. Reis, Macromol. Biosci. 4 (2004) 743–765.

[48] I. Martin, S. Miot, A. Barbero, M. Jakob, D. Wendt, J. Biomech. 4 (2007) 750–765.